Extraction of electromagnetic neutron form factors through inclusive and exclusive polarized electron scattering on a polarized ^{3}He target

J. Golak,[1,2] G. Ziemer,[1] H. Kamada,[1,*] H. Witała,[2] and W. Glöckle[1]
[1]*Institut für Theoretische Physik II, Ruhr-Universität Bochum, D-44780 Bochum, Germany*
[2]*Institute of Physics, Jagellonian University, PL-30059 Cracow, Poland*
(Received 9 August 2000; published 22 February 2001)

Data for the inclusive process $\overrightarrow{^3\mathrm{He}}(\vec{e},e')$ have been theoretically analyzed and values for the magnetic and electric neutron form factors have been extracted at $Q^2=0.1$ and 0.2 GeV$^2/c^2$. Similarly a theoretical analysis has been carried through for the process $\overrightarrow{^3\mathrm{He}}(\vec{e},e'n)$ and the value of the electric neutron form factor has been extracted around $Q^2=0.4$ GeV$^2/c^2$. In both cases the form factor values agree well with the ones extracted from processes on the deuteron. Our results are based on Faddeev solutions, modern *NN* forces, and partially on the incorporation of mesonic exchange currents.

DOI: 10.1103/PhysRevC.63.034006 PACS number(s): 21.45.+v, 25.10.+s, 24.70.+s, 25.30.Fj

I. INTRODUCTION

Besides the deuteron, polarized ^{3}He appears to be a useful target to extract information on the electromagnetic neutron form factors. This proposal goes back to [1] and has been emphasized again by [2]. It is based on the fact that the principal *S* state dominates the ^{3}He wave function by more than 90% and in this state the polarization is carried solely by the neutron. Needless to say that the knowledge of the electromagnetic form factors of the neutron is basic to get insight into the distribution of charge and magnetization inside the neutron. We refer to [3–8,9] for experimental and theoretical work on that topic extracting information on the neutron form factors. In this paper we would like to give for the first time all the details about our analysis of the experiment [10] on the process $\overrightarrow{^3\mathrm{He}}(\vec{e},e')$ with the aim to extract the magnetic neutron form factor, G_M^n, and analyze a recent experiment [13] on the processes $\overrightarrow{^3\mathrm{He}}(\vec{e},e'n)$ carried out in order to extract the electric neutron form factor, G_E^n. The G_M^n values will be determined at $Q^2=0.1$ and 0.2 GeV$^2/c^2$ and the G_E^n value around $Q^2=0.4$ GeV$^2/c^2$. This theoretical analysis will be based on Faddeev solutions for the 3*N* continuum and the 3*N* bound state belonging to the same 3*N* Hamiltonian. We shall also use realistic *NN* forces. For the inclusive process we carried through an analysis before [14], but now it refers to a new more accurate experiment [10] and also the theory will be improved by including mesonic exchange currents. The analysis [15] of the exclusive experiment by consistent Faddeev solutions for the 3*N* continuum and ^{3}He has not been done before to the best of our knowledge.

In Sec. II we shall investigate the inclusive process and in Sec. III the exclusive one. We close with an outlook in Sec. IV.

*Present address: Forschungszentrum Jülich, Institut für Kernphysik (Theorie), D-52425 Jülich, Germany.

II. EXTRACTION OF THE MAGNETIC FORM FACTOR OF THE NEUTRON

In this section we shall analyze a measurement of $\overrightarrow{^3\mathrm{He}}(\vec{e},e')$ carried through at JLab [10]. We refer to [14] for the detailed theoretical formalism and restrict ourselves to describe only its extensions. That paper will henceforth be cited as I and equations thereof by (I.*). In I we used only a single nucleon current operator. Now we add two-body exchange current operators. The central Faddeev-like equation given in Eq. (I.28) is derived under the assumption that the operator *C* has the form of (I.29). In I this simply meant that *C* is a sum of three single particle operators. However, what really enters the derivation of Eq. (I.28) is, that the operator *C* can be decomposed into three parts such that $C^{(i)}$ is symmetrical under exchange of particles $j\neq k$ with $j\neq i\neq k$. The operator *C* has the physical meaning of a component of the current operator. Thus we can simply add two-body currents, which naturally decompose in a 3*N* system into three parts and therefore $C^{(1)}$ in Eq. (I.28) will be now a sum of two terms:

$$C^{(1)}=C^{(1)}_{\mathrm{sing}}+C^{(23)}_{\mathrm{exch}}. \tag{1}$$

The first term is the single-nucleon current used in I and $C^{(23)}_{\mathrm{exch}}$ is the corresponding component of a two-body current acting on particles 2 and 3. As a consequence there will occur now an additional driving term in Eq. (I.28) of the form $(1+tG_0)C^{(23)}_{\mathrm{exch}}|\Psi_{^3\mathrm{He}}m\rangle$.

The following steps in I concern the partial wave representation. Since the spherical components $C^{(23)}_{\pm 1}$ of the two-body current operator are tensor operators and behave like the single nucleon components used in I, the conditions (I.36–37) and as a consequence (I.38) remain valid. The symmetry properties (I.41–44) based on the partial wave decomposed forms remain also valid for the additional two-body currents. This follows from their explicit forms as given in [16]. Then the following expressions leading to the final forms of the four response functions (I.52–55) remain valid.

For the two-body currents we follow the Riska prescription [17], which via the continuity equation relates *NN* forces and exchange currents in a model independent manner, as it is often referred to. We choose the AV18 *NN* force model [18] and restrict ourselves to the dominant π- and ρ-like parts. We refer to [19] for more details and to [16] for the partial wave expansion of the two-body currents. In the case of Bonn B [20], which we also use as another *NN* force model, we choose standard π- and ρ-meson exchange currents augmented by the strong form factors used in Bonn B. For the proton electromagnetic form factors we took the Höhler [25] parametrization, which at $Q^2=0.1$ and 0.2 GeV$^2/c^2$ agrees perfectly with the data.

To theoretically analyze the data from [10] the experimental conditions have to be taken into account. The incoming electron beam energy was $E=778$ MeV. The central electron scattering angles for $Q^2=0.1$ and 0.2 GeV$^2/c^2$ were $\theta_e=24.44°$ and 35.5°, respectively. The spread in the electron angles were $\Delta\theta_e=\pm 1.6°$, and $\Delta\phi_e=\pm 3.4°$. For $Q^2=0.1(0.2)$ GeV$^2/c^2$ or values close to it the virtual photon energies were chosen between 30–90 MeV (80–140 MeV) with a central value of 60 MeV (110 MeV). Each of these two ω ranges were divided into seven bins of length 10 MeV.

The threefold cross section for inclusive scattering has the well-known form [Eq. (I.3)]

$$\frac{d^3\sigma}{d\hat{k}'dk_0'}=\sigma_{\rm Mott}\{v_L R^L+v_T R^T+h(v_{TL'}R^{TL'}+v_{T'}R^{T'})\}. \tag{2}$$

Here $\sigma_{\rm Mott}$ is the Mott cross section, v_i are analytically known kinematical factors and the R^i are inclusive response functions divided into two groups. The first one is present for unpolarized electrons, the second one goes with the helicity h of the electron beam. The primed response functions also depend on the orientation of the ^{3}He spin in relation to the photon direction [see Eqs. (I.56–57)]. The corresponding angles are denoted by $\theta^\star$ and $\phi^\star$. The cross section in Eq. (2) was averaged over the 10 MeV wide ω bins and over the angular spread around the central electron scattering angles. In order to perform the averaging a sufficiently fine grid in θ_e and ω has been chosen for which the four response functions have been calculated. This required quite a few hundred solutions of the corresponding Faddeev equations. The actual averaging was performed via a Monte Carlo procedure based on the response functions known on the grid of electron angles and electron energies. This Monte Carlo procedure takes into account the finite momentum and angular acceptance of the experiment.

The asymmetry is defined as

$$A=\frac{\left.\frac{d^3\sigma}{d\hat{k}'dk_0'}\right|_{h=1}-\left.\frac{d^3\sigma}{d\hat{k}'dk_0'}\right|_{h=-1}}{\left.\frac{d^3\sigma}{d\hat{k}'dk_0'}\right|_{h=1}+\left.\frac{d^3\sigma}{d\hat{k}'dk_0'}\right|_{h=-1}}. \tag{3}$$

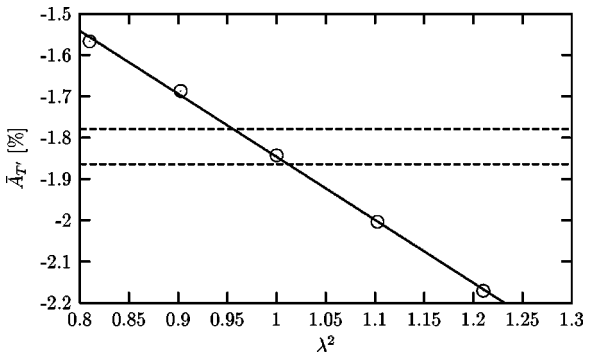

FIG. 1. The averaged asymmetry $\overline{A}_{T'}$ of Eq. (6) around the quasielastic peak against the λ^2 factor for $Q^2=0.1$ GeV$^2/c^2$. The solid curve is a result of a fit. Dashed curves show the experimental bounds for $A_{T'}$.

This ratio is formed out of the averaged cross sections. As a consequence one arrives at [see Eq. (I.58)]

$$A_{average}=\frac{\int d\Omega\,\sigma_{\rm Mott}\{v_{T'}\tilde{R}^{T'}\cos\theta^\star+v_{TL'}\tilde{R}^{TL'}\sin\theta^\star\cos\phi^\star\}}{\int d\Omega\,\sigma_{\rm Mott}\{v_L R^L+v_T R^T\}}\equiv\frac{\Delta}{\Sigma}, \tag{4}$$

where $d\Omega$ stands for the averaging. (We factored off the $\theta^\star\phi^\star$-dependence introducing the response functions with tilde.) For $\theta^\star=0°$ or close to it one focuses on $\tilde{R}^{T'}$ and a corresponding $A_{T'}$, which in a plane wave impulse approximation (PWIA) is essentially proportional to $(G_M^n)^2$ [see Eq. (I.77)]. In the actual experiment one has to live with $\theta^\star\leqslant 10°$ (7.8°) for $Q^2=0.1(0.2)$ GeV$^2/c^2$ and the corresponding $\phi^\star$ is close to 0° or 180°.

The searched for magnetic form factor of the neutron was parametrized as

$$G_M^n(Q^2)\equiv\lambda G_M^n(Q^2)|_{\rm model}, \tag{5}$$

where $G_M^n(Q^2)|_{\rm model}$ was taken from [25]. In order to keep the computer time below an acceptable limit the averaging process was performed only for $\lambda=1$. For the λ values in the neighborhood of 1 it was assumed that the change for $A_{T'}$ from point geometry (fixed ω and central electron angles) to the averaged case is the same as for $\lambda=1$. Because of the smallness of the λ interval around $\lambda=1$ (see below) this is highly plausible. In this manner one generated for each

TABLE I. Our results for G_M^n as a function of Q^2; the uncertainties are statistical and systematic.

Q^2 (GeV/c)^2	G_M^n/G_M^n(dipole)	Uncertainties
0.1	0.966	$\pm 0.014\pm 0.01$
0.2	0.962	$\pm 0.013\pm 0.01$

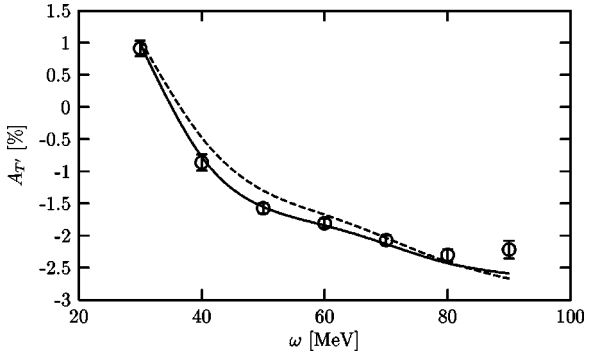

FIG. 2. The asymmetry $A_{T'}$ against the energy transfer ω for $Q^2=0.1$ GeV$^2/c^2$. The curves describe full (averaged) Bonn B predictions with the single nucleon current (dashed) and with the single nucleon current plus the π- and ρ-MEC (solid). Data are from [10].

λ-value theoretical $A_{T'}$ values according to the seven ω bins. The final step is the adjustment of the magnetic form factor of the neutron, G_M^n. Out of the seven ω-bins three central values in the QFS region were selected (for $Q^2=0.1$ GeV$^2/c^2$ $\omega=50$, 60, 70 MeV, and for $Q^2=0.2$ GeV$^2/c^2$ $\omega=100$, 110, 120 MeV) and an additional averaging was performed

$$\overline{A}\equiv\frac{\sum_{j=1}^{3}A_j\Sigma_j}{\sum_{i=1}^{3}\Sigma_i}=\sum_{j=1}^{3}\frac{\Delta_j}{\Sigma_j}\frac{\Sigma_j}{\sum_{i=1}^{3}\Sigma_i}\equiv\sum_{j=1}^{3}\frac{\Delta_j}{\Sigma_j}w_j=\sum_{j=1}^{3}A_jw_j. \tag{6}$$

The indices i and j refer to the three experimental bins. In the third equality weight factors w_j are introduced, which in the actual performance were taken from the experiment (counts related to the unpolarized cross section).

In this manner one arrives at the λ^2 dependence of $\overline{A}$, which turned out to be rather close to a straight line. This is depicted in Fig. 1 for $Q^2=0.1$ GeV$^2/c^2$ together with the experimental values. The case $Q^2=0.2$ GeV$^2/c^2$ is similar. One reads off the λ values leading to the G_M^n values as given in Table I. There our results in the units of G_M^n(dipole) $=\mu_n/(1+Q^2/0.71)^2$ are shown, where μ_n is the magnetic moment of the neutron. They were already published in [10].

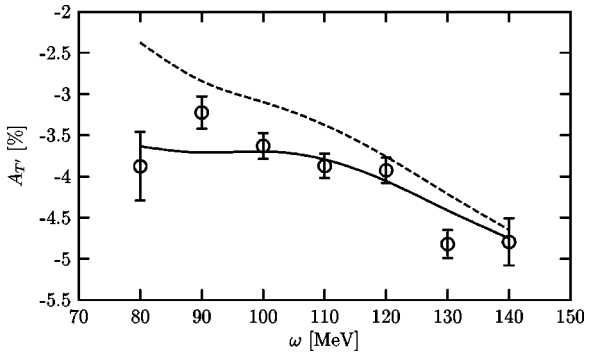

FIG. 3. The same as in Fig. 2 for $Q^2=0.2$ GeV$^2/c^2$.

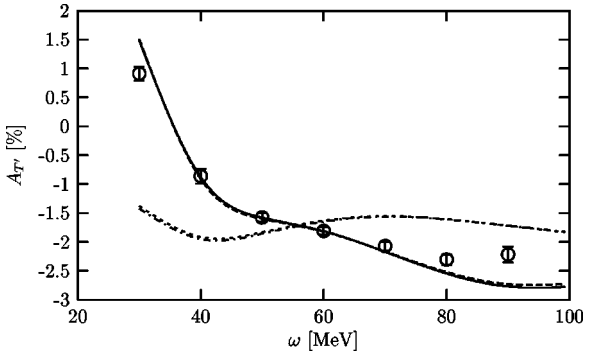

FIG. 4. The asymmetry $A_{T'}$ against the energy transfer ω for $Q^2=0.1$ GeV$^2/c^2$. The curves describe PWIA point geometry results with $G_E^n=0$ (dashed-dotted), and $G_E^n\neq 0$ (dotted); full point geometry results with $G_E^n=0$ (dashed) and $G_E^n\neq 0$ (solid). All results are obtained with the AV18 potential. The single nucleon current plus the π- and ρ-MEC is used. Data are from [10].

Having adjusted G_M^n we can display the ω dependence of $A_{T'}$ in Figs. 2 and 3 in comparison to the experimental values. We see an essentially perfect agreement between theory and experiment. We also show the theoretical result without MEC's but including the full final state interaction. Clearly the MEC's provide an important shift and should not be neglected. Also the final state interaction itself plays a very important role since the PWIA result (see Figs. 4 and 5) is far off. Note our PWIA neglects all final state interactions.

The electric form factor of the neutron, G_E^n, is not yet very well known (see Sec. III), but enters into our calculation. Its effect is totally negligible as can be seen in Figs. 4 and 5. There we compare $A_{T'}$ (for point geometry) evaluated with G_E^n according to [25] and putting it to zero.

For point geometry we also performed full fledged calculations based on the AV18 *NN* force [18] and the π- and ρ-like exchange currents according to the Riska prescription [17]. Both calculations, for Bonn B and AV18 agree very well as shown in Figs. 6 and 7.

Finally we mention that we also included π- and ρ-exchange currents with an intermediate Δ (in a static approximation). Their effects was very small and lead to an estimated change of G_M^n by less than 2%.

The data in Figs. 2–7 are radiatively corrected. This thorough procedure was performed with the help of numerous

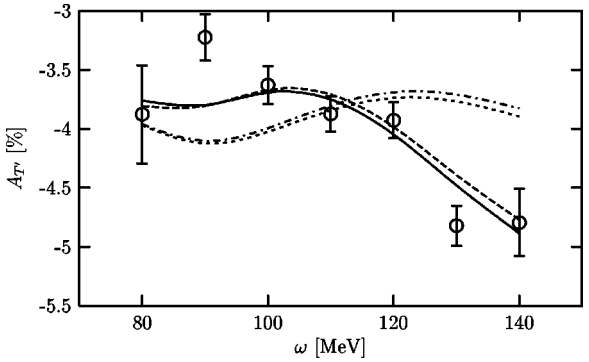

FIG. 5. The same as in Fig. 4 for $Q^2=0.2$ GeV$^2/c^2$.

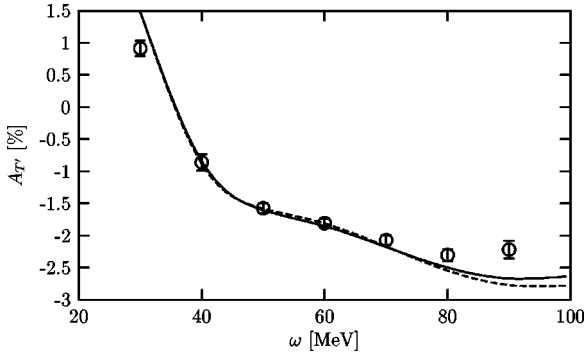

FIG. 6. The asymmetry $A_{T'}$ against the energy transfer ω for $Q^2=0.1$ GeV$^2/c^2$. The curves describe full point geometry results obtained with the AV18 potential (dashed) and with the Bonn B potential (solid). In both cases the single nucleon current plus the π- and ρ-MEC are used. Data are from [10].

full fledged Faddeev calculations and will be described in a separate paper [26].

Our G_M^n values extracted from that inclusive experiment on ^{3}He at $Q^2=0.1$ and 0.2 GeV$^2/c^2$ and published before in [10] agree very well with results achieved in recent experiments on the deuteron [7,8]. This is shown in Fig. 8 together with other data.

We refrained from a theoretical analysis of data taken in the same experiment at higher Q^2 values [10], since one has to expect that relativity will play a non-negligible role. This is left to a future investigation.

III. EXTRACTION OF THE ELECTRIC FORM FACTOR OF THE NEUTRON

In this section we shall analyze a measurement of $\overrightarrow{^3\mathrm{He}}(\vec{e},e'n)$ carried through at MAMI [13] with the aim to extract G_E^n. Our theoretical formalism has been described in [21]. Nevertheless to clearly shed light onto the reactions going on after the virtual photon has been absorbed we would like to lay out the multiple rescatterings and their summation into a Faddeev-like integral equation. In the literature erroneously often just the very first few terms are taken into account. In a graphical representation the full photon-induced breakup process is an infinite sum of the type shown in Fig. 9. We assumed the absorption of the

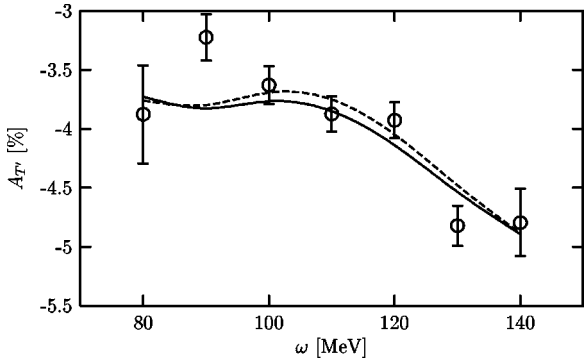

FIG. 7. The same as in Fig. 6 for $Q^2=0.2$ GeV$^2/c^2$.

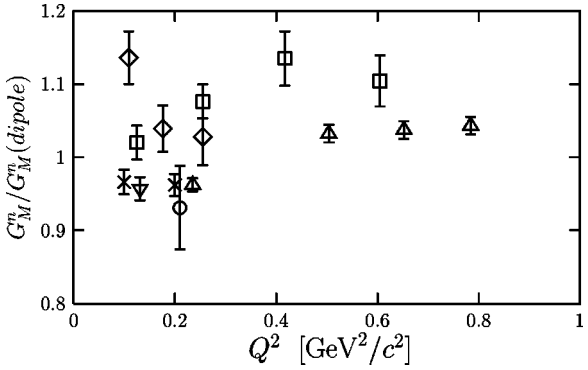

FIG. 8. G_M^n values extracted from different measurements on the deuteron [[27] ($\diamond$), [7] ($\triangledown$), [28] ($\square$), [8] ($\triangle$)] and on ^{3}He [[29] ($\bigcirc$), [10] ($\times$)]. The results of the present analysis were published previously in [10]. The Q^2 points of [7,29] are slightly shifted for clarity.

photon on a single nucleon. Obviously the diagrams can be generalized by photon absorption processes on two or three nucleons. This infinite sequence of processes has its algebraic counterparts

$$N=[j(1)+j(2)+j(3)]|\Psi_{^3\mathrm{He}}\rangle+(t_{12}+t_{23}+t_{31}) \times G_0[j(1)+j(2)+j(3)]|\Psi_{^3\mathrm{He}}\rangle + \sum_{i=1}^{3}\sum_{k<l}\sum_{m<n\neq k<l} t_{mn}G_0t_{kl}G_0j(i)|\Psi_{^3\mathrm{He}}\rangle+\cdots. \quad (7)$$

It is convenient to introduce the notation $t_{ij}\equiv t_k$ ($ijk=123$, etc.) and $P\equiv P_{12}P_{23}+P_{13}P_{23}$. Then it requires little work to put Eq. (7) into the form

$$N=(1+P)j(1)|\Psi_{^3\mathrm{He}}\rangle+(1+P)t_1G_0(1+P)j(1)|\Psi_{^3\mathrm{He}}\rangle + (1+P)t_1G_0Pt_1G_0(1+P)j(1)|\Psi_{^3\mathrm{He}}\rangle+\cdots. \quad (8)$$

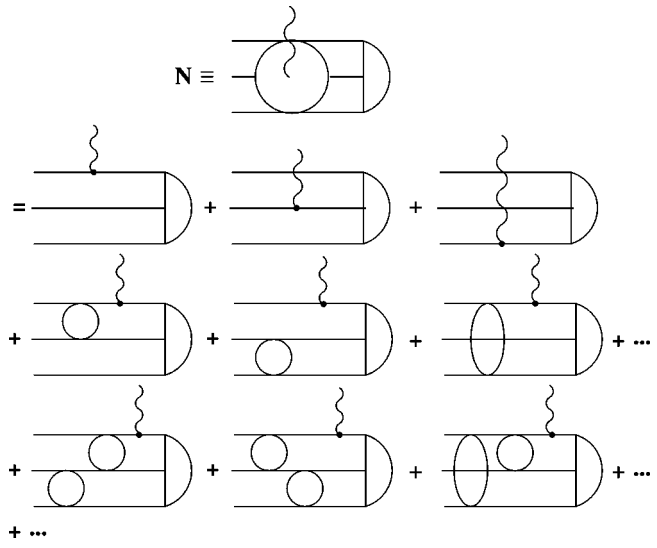

FIG. 9. The multiple rescattering series for the process ^{3}He$(e,e'n)$. The half moon stands for the ^{3}He state, the wavy line for the photon, horizontal lines for freely propagating nucleons, and the ovals for *NN t* matrices. The dots in the third line stand for processes, where the photon is absorbed on the other two nucleons.

The first term contains no final state interaction and we split off, what we shall call plane wave impulse approximation (PWIA),

$$N^{\mathrm{PWIA}} \equiv j(1)|\Psi_{^3\mathrm{He}}\rangle \tag{9}$$

and call the whole term

$$N^{\mathrm{PWIAS}} \equiv (1+P)j(1)|\Psi_{^3\mathrm{He}}\rangle, \tag{10}$$

where S stands for full antisymmetrization. All the additional terms contain rescattering contributions of increasing order in the *NN t* operator:

$$\begin{aligned} N^{\mathrm{rescatt}} &\equiv (1+P)[t_1G_0 + t_1G_0Pt_1G_0 + \cdots] \\ &\quad \times (1+P)j(1)|\Psi_{^3\mathrm{He}}\rangle \\ &\equiv (1+P)|U\rangle. \end{aligned} \tag{11}$$

A more general inspection reveals that

$$\begin{aligned} |U\rangle &= (1 + t_1G_0P + t_1G_0Pt_1G_0P + \cdots) \\ &\quad \times t_1G_0(1+P)j(1)|\Psi_{^3\mathrm{He}}\rangle, \end{aligned} \tag{12}$$

where inside the bracket the operator sequence t_1G_0P occurs in increasing powers. As an immediate consequence one derives

$$|U\rangle = t_1G_0(1+P)j(1)|\Psi_{^3\mathrm{He}}\rangle + t_1G_0P|U\rangle, \tag{13}$$

which is the central integral equation for the amplitude $|U\rangle$. Via Eq. (11) it provides the whole rescattering amplitude [up to the symmetrization $(1+P)$]. This integral equation is of the Faddeev type because of the typical Faddeev structure of its kernel. The same kernel occurs for 3*N* scattering processes [22], only the driving term is different there.

An often used approximation for quasielastic processes in the literature is

$$N \approx j(1)|\Psi_{^3\mathrm{He}}\rangle + t_{23}G_0j(1)|\Psi_{^3\mathrm{He}}\rangle \equiv N^{\mathrm{FSI23}}. \tag{14}$$

Here antisymmetrization in the final state is neglected and one rescattering in the *NN t*-operator t_{23} is only allowed for the two spectator nucleons (which do not absorb the photon). This amplitude is also sometimes called PWIA, but not in this paper.

Needless to say that the full amplitude, now supplemented by the proper vector indices for the current operator is identical to the standard form of the nuclear matrix element

$$N^{\mu} = \langle \Psi_f^{(-)}| \sum_i j^{\mu}(i)|\Psi_{^3\mathrm{He}}\rangle. \tag{15}$$

We refer to [21] for the verification.

The sixfold differential cross section for the exclusive process under discussion has the well-known form [23]

$$\begin{aligned} \frac{d^6\sigma}{d\hat{k}'\,dk_0'\,d\hat{p}_n\,dp_n} &= \sigma_{\mathrm{Mott}}p_n^2\frac{pm_N}{2}\int d\hat{p}\{v_LR^L + v_TR^T + v_{TT}R^{TT} \\ &\quad + v_{TL}R^{TL} + h(v_{TL'}R^{TL'} + v_{T'}R^{T'})\}. \end{aligned} \tag{16}$$

TABLE II. Intervals for the neutron momenta.

θ_e (deg)	p_n^{min} (MeV/c)	p_n^{max} (MeV/c)
39	500.31	598.68
40	507.60	609.08
41	515.14	619.88
42	522.93	631.15
43	530.99	642.90
44	539.33	655.18
45	547.98	668.00
46	556.94	681.43
47	566.24	695.52
48	575.91	704.73
49	585.95	714.23
50	596.40	724.04
51	607.28	734.18
52	618.65	744.66
53	630.51	755.50
54	642.90	766.74
55	651.02	772.61
56	659.38	778.61
57	668.00	784.69
58	676.90	790.91
59	686.06	797.24

Here $\hat{k}'$, k_0', $\hat{p}_n$, p_n, p, $\hat{p}$ in turn are the unit vector in the direction of the scattered electron, its energy, the unit vector of the knocked out neutron, its momentum, the magnitude of the relative momentum of the undetected two protons and finally the unit vector pointing into the direction of that relative momentum.

Throughout this paper we use a strictly nonrelativistic notation.

The information on G_E^n magnified by the product with G_M^n is contained in $R_{TL'}$ as can be explicitly seen working out PWIA [15] (see also [13]). In order to isolate the primed structure functions one forms an asymmetry A of the cross section with respect to the electron helicities $h = \pm 1$. One finds the well-known result

$$A = \frac{\int d\hat{p}(v_{TL'}R^{TL'} + v_{T'}R^{T'})}{\int d\hat{p}(v_LR^L + v_TR^T + v_{TT}R^{TT} + v_{TL}R^{TL})}. \tag{17}$$

In the experiment two perpendicular polarization axis for the spin of ^{3}He have been chosen, $\vec{S}_{\parallel}$ and $\vec{S}_{\perp}$, leading to $A_{\parallel}$ and $A_{\perp}$. In an optimal set up $\vec{S}_{\parallel}$ and $\vec{S}_{\perp}$ would be parallel and perpendicular to the direction of the virtual photon. Then it is well known from the expression for PWIA that under this approximation

$$\frac{A_{\perp}}{A_{\parallel}} \propto \frac{G_E^n}{G_M^n}. \tag{18}$$

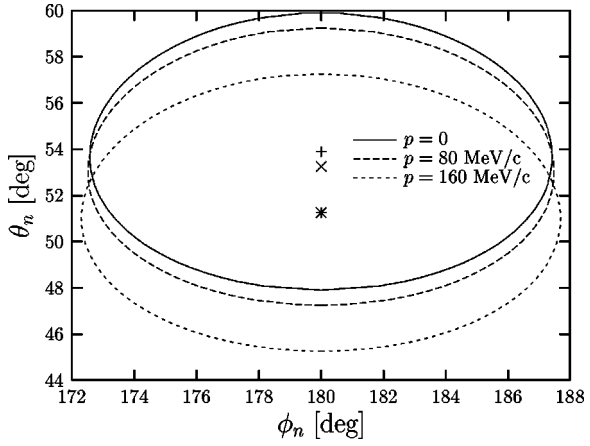

FIG. 10. Integration limits for $\hat{p}_n$ (solid curve) for the example $\theta_e=43°$, $\phi_e=0°$, and $p_n=530$ MeV/c together with the direction of the photon $+$. The dashed and dotted curves are for $p=80$ and 160 MeV/c and the corresponding directions of the photon are given by $\times$ and $*$.

Therefore the aim will be to extract G_E^n from the measured value of that ratio. This is under the assumption that G_M^n is sufficiently well known. Our contribution in this paper is to show that the final state interaction (FSI) does not wash out the signal for G_E^n and that taking FSI into account is crucial.

We shall now describe the experimental conditions under which the data were taken. The electron and neutron detectors covered a wide range of angles. We refer to [12,15] for the detailed information and provide here only approximate values: $40°\leqslant\theta_e\leqslant 60°$, $-15°\leqslant\phi_e\leqslant 15°$, $35°\leqslant\theta_n\leqslant 65°$, $160°\leqslant\phi_n\leqslant 200°$. Depending on the electron scattering angle θ_e only neutron momenta within certain cuts were accepted as shown in Table II. Since the energy of the scattered electron was not measured (except for excluding pion-production) the direction of the virtual photon was not known. However it was possible to correlate the directions of the photon and the knocked out neutron in the following manner [11]. Take the relative momentum p of the two undetected protons to be zero. Then for fixed values of $\hat{k}'$, $\hat{p}_n$, and p_n, k_0' and therefore $\vec{Q}$, the virtual photon momentum, follow kinematically. Now only those angles were allowed such that the angle between $\vec{Q}$ and $\hat{p}_n$ was smaller or equal to 6°. In our theoretical analysis we also took that experimentally chosen constraint into account. As an example we show in Fig. 10 the allowed region for the neutron angles for given values of $\theta_e=43°$, $\phi_e=0°$, $p_n=530$ MeV/c, and $p=0$ (solid curve). In reality there is a distribution of p values; see Fig. 11 below. Consequently for that region of neutron angles also other events with $p\neq 0$ contribute, which belong to different directions of $\vec{Q}$. This is also shown in Fig. 10. In the worst case the angle between $\hat{Q}$ and $\hat{p}_n$ can be as large as 9° for the tails of the p distribution.

Since the energy of the scattered electron has not been measured the cross section reduces to a fivefold one

$$\frac{d^5\sigma}{d\hat{k}'d\hat{p}_n dp_n}=\frac{m_N}{2}\sigma_{\rm Mott}p_n^2\int dk_0' p\int d\hat{p}\{v_L R^L+v_T R^T + v_{TT}R^{TT}+v_{TL}R^{TL}+h(v_{TL'}R^{TL'}+v_{T'}R^{T'})\}. \tag{19}$$

We convert the k_0' integration into one over p, take into account the experimental acceptances and end up with the summed up cross section

$$\begin{aligned}\Delta\sigma &\equiv \int_{\Delta\hat{k}'}d\hat{k}'\,\sigma_{\rm Mott}\int_{\Delta p_n}dp_n p_n^2\int_{\Delta\hat{p}_n}d\hat{p}_n\int d\vec{p}\rho\{v_L R^L \\ &\quad + v_T R^T+v_{TT}R^{TT}+v_{TL}R^{TL}+h(v_{TL'}R^{TL'}+v_{T'}R^{T'})\} \\ &\equiv \int d\Omega\{v_L R^L+v_T R^T+v_{TT}R^{TT}+v_{TL}R^{TL} \\ &\quad + h(v_{TL'}R^{TL'}+v_{T'}R^{T'})\}.\end{aligned} \tag{20}$$

In our nonrelativistic formulation ρ has the form

$$\rho=\frac{2m_N p^2}{\sqrt{(k\cos\theta_e-\vec{p}_n\cdot\hat{k}'-2m_N)^2+4m_N(k+\epsilon_{^3\rm He})-4p^2-3p_n^2-k^2+2\vec{p}_n\cdot\vec{k}}}. \tag{21}$$

Since we shall form asymmetries there is no need to determine the value of the covered phase space. Using $\Delta\sigma$ for the two ^{3}He-spin directions one can form the two asymmetries $A_\perp$, $A_\parallel$ for the $\perp$ and $\parallel$ orientations of the ^{3}He spin and finally their ratio V

$$V\equiv\frac{A_\perp}{A_\parallel}=\frac{\int d\Omega(v_{TL'}R^{TL'}+v_{T'}R^{T'})_\perp}{\int d\Omega(v_{TL'}R^{TL'}+v_{T'}R^{T'})_\parallel}\times 1. \tag{22}$$

The ''1'' in Eq. (22) denotes the corresponding ratio for the helicity independent parts of $\Delta\sigma$. It turned out that this latter ratio was extremely close to 1 (within less than 0.1%).

Before we shall present our results for V as a function of a parametrization of G_E^n we would like to give some insight into the functions entering Eq. (22). For some fixed directions of $\hat{k}'$ and $\hat{p}_n$ and some value of p_n contained in the domain Ω we define the quantities

$$\Lambda_\beta^\alpha\equiv\int d\hat{p}R_\beta^\alpha, \tag{23}$$

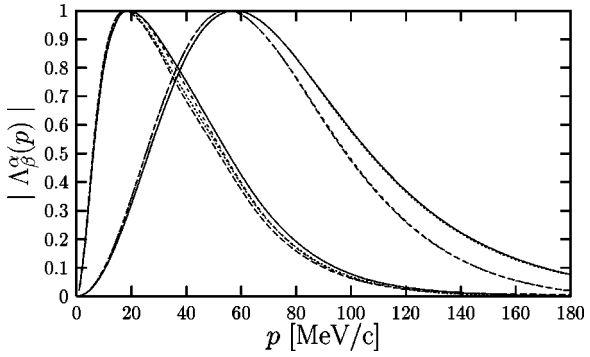

FIG. 11. The magnitudes of the $\Lambda_{\parallel}^{T'}(p)$ (solid), $\Lambda_{\parallel}^{TL'}(p)$ (long dashed), $\Lambda_{\perp}^{T'}(p)$ (short dashed), and $\Lambda_{\perp}^{TL'}(p)$ (dotted) amplitudes of Eq. (23) as a function of p. They are all arbitrarily normalized to 1 at their maxima and correspond to the arbitrarily chosen values of $\theta_e=43°$, $\phi_e=0°$, $\theta_n=53.9°$, $\phi_n=180°$, and $p_n=530$ MeV/c. The group of curves peaking at $p\approx 20$ MeV/c (60 MeV/c) refers to full FSI (PWIA).

which depend on p. For α we choose T' and TL' and β corresponds to $\perp$ and $\parallel$ orientations of the ^{3}He spin. Figure 11 tells us that indeed the distribution of the p values is peaked at low values, where the maxima occur at kinetic energy values of relative motion of the two protons of about 0.4 MeV. At around 140 MeV/c the p distribution has essentially vanished. Those curves in Fig. 11 refer to full FSI. In contrast the corresponding curves for PWIA, also displayed in Fig. 11, show a much wider p distribution, which has intriguing consequences as described below.

Next let us choose a fixed k_0' value, $k_0'=650$ MeV/c, and again fixed angles $\theta_e=40°$, $\phi_e=0°$, $\theta_n=49.48°$, and $\phi_n=180°$ all chosen out of the large domain Ω. In Fig. 12 we display the magnitudes of one of the amplitudes $\Lambda_{\perp}^{T'}$, now as a function of p_n. The others are qualitatively similar. We compare different approximate treatments of the final state to the full calculation. The pure PWIA drops strongly with decreasing p_n. This is a simple consequence of the fact that the ^{3}He wave function drops with increasing momenta. Choosing Jacobi momenta as arguments of the ^{3}He wave function the photon momentum $\vec{Q}$ enters as $\vec{q}=\vec{p}_n-\vec{Q}$, where $\vec{q}$ is the relative momentum of the neutron in relation to the two protons. The decrease of the ^{3}He wave function with increasing q explains the PWIA curve in Fig. 12. In case of the symmetrized PWIAS the photon can also be absorbed by the two protons, which leads to $\vec{q}=\vec{p}_n$ and the occurrence of $\vec{Q}$ in the other Jacobi momentum $\vec{p}_{23}$ as $\vec{p}_{23}=\vec{p}\mp\frac{1}{2}\vec{Q}$. As a consequence the two additional amplitudes in PWIAS start to contribute at lower p_n values, which can clearly be seen in Fig. 12. The curve denoted as FSI23 is based on the final state interaction among the two final protons. This reduced final state interaction has apparently a strong effect even near the quasielastic peak. Again including full antisymmetrization in the final state, but keeping only a first order final state interaction, leads to strong deviations at low neutron momenta. This is denoted by FSI23S. Finally the full FSI (including of course antisymmetrization in the final state) leads to a behavior, which is similar to FSI23 near the upper end of p_n but deviates then from all other curves for lower p_n values.

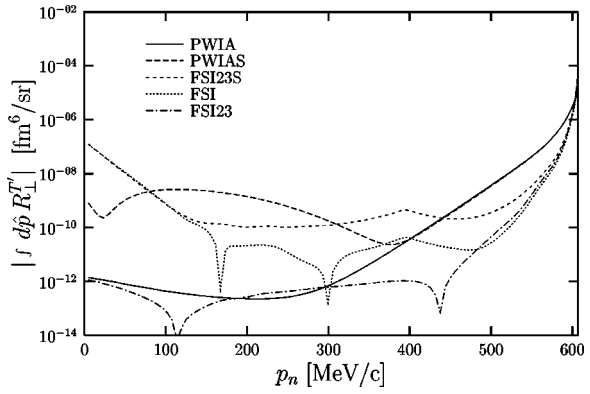

FIG. 12. FSI effects in the integrated response function $R^{T'}$.

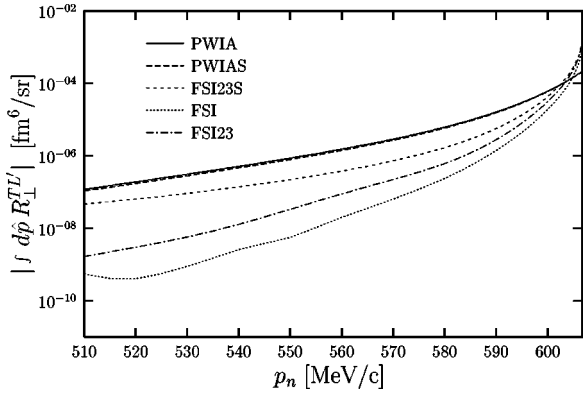

FIG. 13. The same as in Fig. 12 for the truncated p_n region used in the analysis of the experiment [13] and for the response function $R^{TL'}$.

Since the experiment under discussion emphasizes the large p_n values in accordance with at least approximate quasifree scattering conditions, we display in Fig. 13 as an example the magnitude of one of the four Λ_{β}^{α} amplitudes restricted to the domain seen in the experiment. We see a coincidence of PWIA and PWIAS in the restricted p_n interval and a spread of curves for the other predictions. Especially the FSI is clearly distinct from FSI23. The other three Λ_{β}^{α} amplitudes show a similar behavior but the magnitudes can be quite different [15].

The ratios of asymmetries for point geometries inside the domain Ω vary very much and depend extremely strongly on the treatment of the final $3N$ state. One more or less arbitrarily chosen case is displayed in Fig. 14. We see the ratio for PWIA, PWIAS, FSI23, FSI, and an additional case, FSIn. In the latter case we put the electric form factor of the proton, G_E^p, to zero (the contribution of G_M^p is insignificant [15]). This has been done to demonstrate the presence and importance of the photon absorption on the two protons. Corresponding curves drawn for other point geometries inside the domain Ω show dramatic variations [15]. Consequently averaging over asymmetries related to point geom-

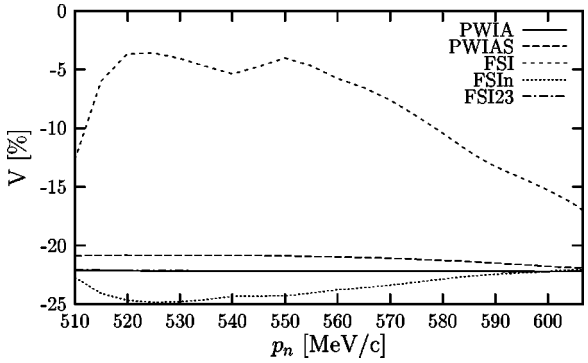

FIG. 14. Ratios V for point geometry ($k_0'=650$ MeV/c, $\theta_e=40°$, $\theta_n=49.48°$, $\theta_\parallel^\star=1.12°$, $\theta_\perp^\star=88.88°$, $|\vec{Q}|=549.61$ MeV/c) for various treatments of the final state against p_n.

etries is not advisable. Instead summing up cross sections first as in Eq. (20) and then forming asymmetries is what has to be done.

Let us now show our results for the ratio of asymmetries given in Eq. (22). We parametrize G_E^n by multiplying three models for G_E^n by a factor λ. We choose the ones by Gari-Krümpelmann [24]. Figure 15 shows various theoretical ratios V against λ in comparison to the experimental value of $V^{\rm exp}=(-7.26\pm1.14)\%$ [12,13]. The largest λ-value results for FSI, followed by PWIAS, then PWIA and finally FSI23. The four results for $G_E^n\equiv\lambda\cdot G_E^n|_{\rm model}$ are plotted in Fig. 16 in the range of Q^2 values touched in that experiment. This refers to one of the three models. The others are very similar. Finally we show in Fig. 17 G_E^n as extracted through FSI and including the spread caused by the experimental error. Superimposed on the spread caused by the experimental error we see small variations due to the three different choices of G_E^n models. For the central values around $Q^2=0.4$ GeV$^2/c^2$ that model dependence is totally negligible. This figure displays our result for G_E^n in the Q^2 range covered by the experiment based on the functional form of Gari-Krümpelmann [24] and extracted from one experimental value for the ratio V. It is documented also in Table III in the last line (''FSI''), where we have taken the average of the highest and lowest values in Fig. 17. The other numbers in Table III are corresponding averages for the various approximate treatments of the 3N final state and are given only as

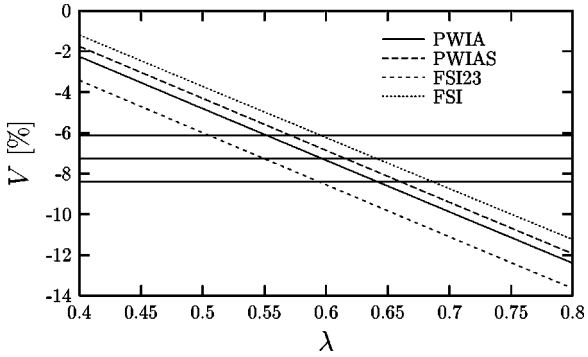

FIG. 15. Theoretical ratios V against λ in comparison to the experimental value including its error.

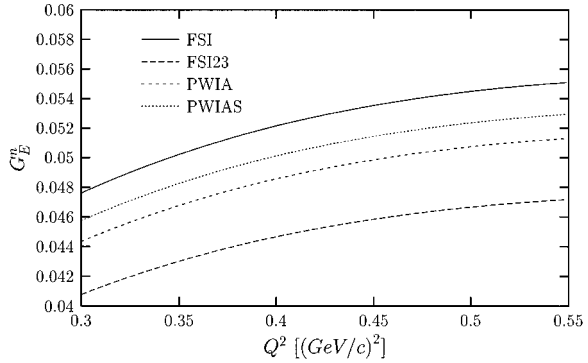

FIG. 16. Extracted G_E^n values for different treatment of the final state.

additional information for the reader. This average takes into account uncertainties of both, model dependence for G_E^n and experimental errors.

Instead of relying on the specific functional Q^2 dependence as given by the Gari-Krümpelmann parametrization [24], we restrict ourselves to show in Fig. 18 one G_E^n value at $Q^2=0.4$ GeV$^2/c^2$, which is the center of the Q^2 domain covered in the experiment. Thus our final result for FSI, $G_E^n=0.052\pm0.0038$ at $Q^2=0.40$ GeV$^2/c^2$, is added in Fig. 18 to the ones extracted from processes on the deuteron. There is a fair agreement. Also added is another result achieved at MAMI [4] at a higher Q^2 value. No FSI corrections have been taken into account in that case.

It is astonishing that PWIAS (and PWIA) are relatively close to the value based on FSI. This is due to an accidental conspiracy. The slower decrease in the p distribution for PWIA(S) shown in Fig. 11 causes smaller energies of the scattered electrons than for FSI. As a consequence the photon-direction deviates more strongly in case of $\vec{S}_\perp$ from 90° than for FSI. This leads to a strongly modified contribution $(\int d\Omega v_{T'}R^{T'})_\perp$ for PWIAS in comparison to using FSI. In addition because of the lacking FSI there are smaller protonic contributions. This together, as a detailed investigation shows [15], yields the accidental result, that PWIAS is close to the full result. The fact that PWIA(S) yields an un-

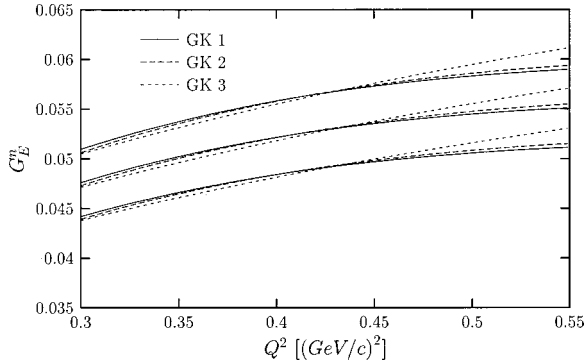

FIG. 17. The extracted G_E^n for full FSI. The three separated curves correspond to the three λ values from Fig. 15. The smaller spread of curves is due to the three different parametrizations of $G_E^n|_{\rm model}$.

TABLE III. Extracted averaged G_E^n values (see text) obtained for different assumptions about the final state. The line ''FSI'' contains our ''best'' G_E^n values according to the full treatment of the final state interaction. The Q^2 dependence is modeled after Gari-Krümpelmann [24]. The uncertainties arise from the spread in the form factor parametrization and the experimental error.

	Q^2 [(GeV/c)^2]		
	0.30	0.35	0.40
PWIA	0.0441±0.0035	0.0465±0.0038	0.0484±0.0038
PWIAS	0.0455±0.0035	0.0480±0.0038	0.0499±0.0038
FSI23	0.0406±0.0035	0.0428±0.0037	0.0446±0.0038
FSI	0.0474±0.0036	0.0499±0.0038	0.0520±0.0038
	Q^2 [(GeV/c)^2]		
	0.45	0.50	0.55
PWIA	0.0500±0.0039	0.0512±0.0043	0.0523±0.0049
PWIAS	0.0515±0.0038	0.0529±0.0043	0.0539±0.0049
FSI23	0.0460±0.0038	0.0472±0.0043	0.0482±0.0048
FSI	0.0536±0.0039	0.0550±0.0044	0.0561±0.0050

realistic result could be verified by measuring the p distribution for the response functions.

Our present result leaves room for improvement. The effect of MEC's like in Sec. II is still to be explored and due to the relatively high Q^2 value one cannot exclude that relativistic effects might be noticeable. This is left to future investigations.

IV. SUMMARY AND OUTLOOK

We have extracted from two measurements on $\overrightarrow{^3\mathrm{He}}(\vec{e},e')$ and $\overrightarrow{^3\mathrm{He}}(\vec{e},e'n)$ the magnetic and electric neutron form factors at certain Q^2 values. Our results are based on consistent Faddeev solutions for the 3N continuum and the 3N bound state. Modern NN forces have been used. In case of the inclusive reaction leading to G_M^n we added π- and ρ-like two-body exchange currents to the single nucleon current. Their effects were substantial. In the exclusive process only a single nucleon current operator has been used, which leaves room for improvement. In both cases a strictly nonrelativistic formulation has been used, which also should be improved.

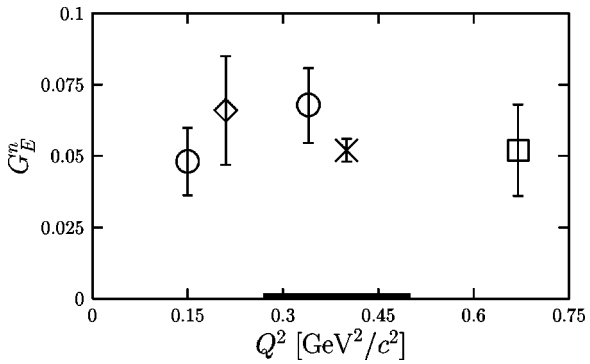

FIG. 18. G_E^n values extracted from ^{3}He [this work (×), [4] (□)] and from processes on the deuteron [[5] (◇), [6] (○)]. The Q^2 range covered in experiment [13] is indicated by a bold horizontal line.

Our values for G_M^n and G_E^n agree well with the values extracted from processes on the deuteron.

From 3N scattering it is known that the most modern data-equivalent NN forces lead in nearly all cases to results, which are very close together. We consider this robustness to be an important insight which gives confidence to those choices of the 3N Hamiltonian. In the case of photon-induced processes a corresponding verification of robustness against interchanges of NN forces and consistent MEC's is still missing. This refers not only to the 3N system but to the 2N system as well. Also generally accepted and feasible relativistic formalisms have still to be worked out.

ACKNOWLEDGMENTS

This work was supported by the Deutsche Forschungsgemeinschaft (J.G. and H.K.), the Polish Committee for Scientific Research, and the Science and Technology Cooperation Germany-Poland. One of us (W.G.) would like to thank the Foundation for Polish Science for the financial support during his stay in Cracow. We would like to thank Dr. H. Gao and Dr. D. Dutta for providing us with detailed information about their experiment and data analysis. The numerical calculations have been performed on the PVP machines of the NERSC, U.S.A., on the Cray T90 of the NIC in Jülich, Germany, and on the VPP300 machine of the RWTH in Aachen, Germany.

[1] B. Blankleider and R. M. Woloshyn, Phys. Rev. C **29**, 538 (1984).
[2] J. L. Friar, B. F. Gibson, G. L. Payne, A. M. Bernstein, and T. E. Chupp, Phys. Rev. C **42**, 2310 (1990).
[3] C. W. de Jager, in *Bates 25: Celebrating 25 Years of Beam to Experiment*, edited by T. W. Donnelly and W. Turchinetz, AIP Conf. Proc. No. 520 (AIP, Melville, NY, 2000), p. 225.
[4] D. Rohe *et al.*, Phys. Rev. Lett. **83**, 4257 (1999).
[5] I. Passchier *et al.*, Phys. Rev. Lett. **82**, 4988 (1999).
[6] C. Herberg *et al.*, Eur. Phys. J. A **5**, 131 (1999).
[7] H. Anklin *et al.*, Phys. Lett. B **336**, 313 (1994).
[8] H. Anklin *et al.*, Phys. Lett. B **428**, 248 (1998).
[9] A. Kievsky, E. Pace, G. Salme, and M. Viviani, Phys. Rev. C **56**, 64 (1997); C. Ciofi degli Atti, E. Pace, and G. Salme, *ibid.* **46**, R1591 (1992); **51**, 1108 (1995); R. W. Schultze and P. U. Sauer, *ibid.* **48**, 38 (1993).
[10] W. Xu *et al.*, Phys. Rev. Lett. **85**, 2900 (2000).
[11] J. Becker and P. Grabmayr (private communication).
[12] J. Becker, Ph.D. thesis, Johannes Gutenberg University, Mainz, 1997.
[13] J. Becker *et al.*, Eur. Phys. J. A **6**, 329 (1999).
[14] S. Ishikawa, J. Golak, H. Witała, H. Kamada, W. Glöckle, and D. Hüber, Phys. Rev. C **57**, 39 (1998).
[15] G. Ziemer, Ph.D. thesis, Ruhr-Universität Bochum (in preparation).
[16] V. V. Kotlyar, H. Kamada, J. Golak, and W. Glöckle, Few-

Body Syst. **28**, 35 (2000).
[17] D. O. Riska, Phys. Scr. **31**, 107 (1985); **31**, 471 (1985).
[18] R. B. Wiringa, V. G. J. Stoks, and R. Schiavilla, Phys. Rev. C **51**, 38 (1995).
[19] J. Golak, H. Kamada, H. Witała, W. Glöckle, J. Kuroś, R. Skibiński, V. V. Kotlyar, K. Sagara, and H. Akiyoshi, Phys. Rev. C **62**, 054005 (2000).
[20] R. Machleidt, Adv. Nucl. Phys. **19**, 189 (1989).
[21] J. Golak, H. Kamada, H. Witała, W. Glöckle, and S. Ishikawa, Phys. Rev. C **51**, 1638 (1995).
[22] W. Glöckle, H. Witała, D. Hüber, H. Kamada, and J. Golak, Phys. Rep. **274**, 107 (1996).
[23] T. W. Donnelly and A. S. Raskin, Ann. Phys. (N.Y.) **169**, 247 (1986).
[24] M. Gari and W. Krümpelmann, Phys. Lett. B **173**, 10 (1989); **274**, 159 (1992); **282**, 483(E) (1992).
[25] G. Höhler, E. Pietarinen, I. Sabba-Stefanescu, F. Borkowski, G. G. Simon, V. H. Walther, and R. D. Wendling, Nucl. Phys. **B114**, 505 (1976).
[26] F. Xiong (in preparation).
[27] P. Markowitz *et al.*, Phys. Rev. C **48**, R5 (1993).
[28] E. E. W. Bruins *et al.*, Phys. Rev. Lett. **75**, 21 (1995).
[29] H. Gao *et al.*, Phys. Rev. C **50**, R546 (1994); H. Gao, Nucl. Phys. **A631**, 170c (1998).